**University of Sunderland**

# Journal Pre-proof

Effects of chemical structure and morphology of graphene-related materials (GRMs) on melt processing and properties of GRM/polyamide-6 nanocomposites

Julio Gomez, Elvira Villaro, Panagiotis G. Karagiannidis, Ahmed Elmarakbi

Please cite this article as: J. Gomez, E. Villaro, P.G. Karagiannidis, A. Elmarakbi, Effects of chemical structure and morphology of graphene-related materials (GRMs) on melt processing and properties of GRM/polyamide-6 nanocomposites, *Results in Materials*, https://doi.org/10.1016/j.rinma.2020.100105.

This is a PDF file of an article that has undergone enhancements after acceptance, such as the addition of a cover page and metadata, and formatting for readability, but it is not yet the definitive version of record. This version will undergo additional copyediting, typesetting and review before it is published in its final form, but we are providing this version to give early visibility of the article. Please note that, during the production process, errors may be discovered which could affect the content, and all legal disclaimers that apply to the journal pertain.

# CRediT author statement

**Julio Gomez:** Conceptualization, Supervision, Methodology, **Elvira Villaro.**: Investigation, Methodology, **Panagiotis G. Karagiannidis**: Writing- Reviewing and Editing, Validation, Formal Analysis. **Ahmed Elmarakbi**: Conceptualization, Supervision.

# Effects of chemical structure and morphology of graphene-related materials (GRMs) on melt processing and properties of GRM/polyamide-6 nanocomposites

Julio Gomez[1*], Elvira Villaro[2], Panagiotis G. Karagiannidis[3], Ahmed Elmarakbi[4].


[1] *Avanzare Innovacion Tecnologica S.L. Av. Lentiscares 4-6, 26370, Navarrete, Spain.*

[2] *Instituto de Tecnologías Químicas de La Rioja (Inter-Química), San Francisco 11, 26370, Navarrete, Spain.*

[3]*School of Engineering, Faculty of Technology, University of Sunderland, Sunderland SR6 0DD, United Kingdom*

[4]*Department of Mechanical and Construction Engineering, Faculty of Engineering and Environment, Northumbria University, Newcastle NE18ST, United Kingdom*


*Corresponding Author - julio@avanzare.es

**ABSTRACT**

In this work, different graphene-related materials (GRMs) and polyamide-6 (PA6) were melt compounded by twin screw extrusion. The GRMs prepared were graphene nanoplatelets (GNPs), graphene oxide (GO), reduced graphene oxide (rGO) and silane functionalised reduced graphene oxide (f-rGO). The GRMs had comparable lateral size (20-30μm), but different thickness and surface chemistry which resulted in different behaviour in processing of melt flow, maximum loading in the PA6 matrix (15%wt for GNPs, 10%wt for GO, 2%wt for rGO and 2.5%wt for f-rGO) as well as mechanical properties. A second extrusion phase
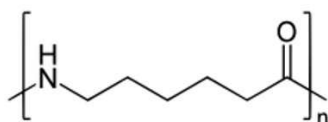
1

produced formulations with lower concentration of GRMs. In the case of f-rGO/PA6, the melt flow index increased by over 76% at 0.5%wt loading compared with the pure PA6 resin, facilitating processing and dispersion of the flakes within the matrix and increasing the elastic modulus and tensile strength by 39%. However, high filler content above 10% has been achieved only for GNPs improving the elastic modulus by 50% at 15%wt.

**Keywords:** graphene, graphene oxide, reduced graphene oxide, functionalisation, polyamide-6, polymer nanocomposites, twin screw extrusion

## 1. Introduction

Polyamide-6 (PA6 or nylon-6) based nanocomposites have been used in automobiles since the 1990's, when Toyota first produced PA6-clay nanocomposites with unprecedented thermomechanical properties[1]. This proved to be the starting point of an intense international academic and industrial research[2]. PA6 (Figure 1) is an appealing thermoplastic with good processability and chemical resistance. The wide application areas of PA6 include automotive components [3], fibers [4], housings for domestic and power tools, electric plugs, and sockets [5], medical implants [6], triboelectric nanogenerators [7] and many others.

A variety of fillers have been used to improve its stiffness, strength [8] and abrasive wear e.g. glass fibers [9], talc [10], calcium carbonate [11], clay minerals [12] [13] [14], organoclays [15] and carbon nanotubes [16], enabling the replacement of heavier metals e.g. in automotive components, such as the intake manifold, cylinder head lid, air filter housing, recirculation system of exhaust gases with valve and oil filtering system [3].

**Figure 1.** Chemical formula of polyamide-6 (PA6 or nylon-6).

Recently, graphene has attracted significant interest as a filler in polymer composites, because it can produce a dramatic improvement in properties at low filler content. As graphene/polymer composites have shown superior mechanical, thermal, electrical, gas barrier, flame retardant and other properties compared to the neat polymers, lots of researchers have been studying graphene/polymer nanocomposites around the world[17] [18] [19] [20]. In recent years, a large number of research studies have been performed on graphene/PA6 as presented by Fu et al. [21]. The most used methods to prepare graphene/PA6 nanocomposites so far are melt blending[22] [23], solvent blending[24] and in situ polymerization[25] [26]. Melt blending is a more practical, versatile and economical technique; mixing is performed in the melt state via industrial processes such as extrusion, injection moulding or melt spinning[21]. However, the resultant properties are inferior because the interaction between graphene and polymer matrix is poor [21]. A good dispersion during melt mixing has proven a challenging problem[27]. Fukushima et al. [28] added 20 %vol graphite nanoplatelets xGnP (xGnP-1 and xGnP-15 with 0.86μm and 1μm lateral size respectively and thickness 5-10nm) into nylon-6 (Durethan B40SK Extrusion Grade, Bayer) and obtained a flexural modulus of about 12 GPa, which was more than 400% over that of the control nylons. However, the authors reported lower flexural strength for xGnP than nanoclay composites, which was attributed to the surface condition of the xGnPs, not optimised for the nylon resulting in low strain debonding of the flakes[28]. Mayoral et al.[29] achieved an increase of up to 412% in the tensile modulus of PA6 (BASF Ultramid B40L) with the addition of 20%wt of GNPs (M-5 and C-500, xGnP®, XG Sciences). To the best of our knowledge, there is no systematic study of melt compounding of different graphene and related materials (GRMs) with PA6, which would determine the optimum GRM surface chemistry, morphology and loading.

3

In this work, we prepared GRMs with different surface chemistry and thickness; that is graphene nanoplatelets (GNPs), graphene oxide (GO), reduced graphene oxide (rGO) and silane functionalised reduced graphene oxide (f-rGO). Following extensive characterisation, various amounts of GRMs were melt blended with PA6, using an industrial and a laboratory twin-screw extruder, both working in contra-rotatory conditions. Our study revealed the different processing behaviour of each type of GRM and mechanical properties of the final nanocomposites. We found a remarkable increase by 67% in the melt flow index (MFI) for the f-rGO at just 0.05%wt loading and improvements in elastic modulus of up to 50% with 15%wt loading of GNPs.

## 2. Experimental part

### 2.1. Materials

PA6 (Ultramid B3K) was supplied by BASF (Germany) in the form of uncoloured pellets with a bulk density □0.7 g/cm³. GNPs were prepared as described by Colonna et al.[30]. GO was prepared according to the Hummers method[31] and modified as described in our previous communication [32]. rGO was prepared from GO by a thermochemical reduction process using ascorbic acid (Vitamin C)[32], which is a very good reducing agent converting the epoxy groups of GO to C=C. Then, the chemically reduced GO was heated in an oven under Ar atmosphere for 20min at 700ºC. f-rGO was prepared as follows; 10g of rGO was suspended in a mixture of ethanol/water (30/70) and stirred for 1 h. Concentrated hydrochloric acid was added to adjust pH between 3-3.5 to hydrolyse the silane, which was added in the following step. 5 mL of (3-aminopropyl) triethoxy-silane (APTES), which can react with groups of the PA6 matrix, were added and the mixture was set at 60ºC, keeping under stirring overnight. The

4

suspension was vacuum filtered to avoid extra silane molecules which have not reacted and washed with ethanol; the powder was dried at 80ºC for 24 h.
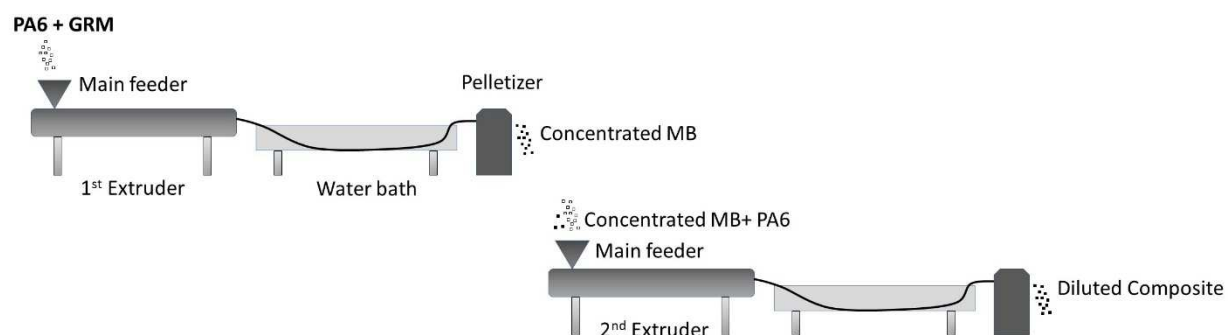
## 2.2 Characterisation of GRMs

The morphology of the GRMs, was studied by Scanning Electron Microscopy (SEM) using a Hitachi S-2400 microscope, Field Emission Scanning Electron Microscopy (FESEM) using a Merlin VP Compact from Zeiss at 1 kV and Transmission Electron Microscopy (TEM) using a JEOL JEM-2010 microscope, equipped with INCA Energy TEM 100 X-ray detector and a GATAN camera (SC600ORIUS). GRM samples were dispersed in isopropyl alcohol, then sonicated with a Hielscher UP200S sonicator for 15 minutes and drop casted onto $Si/SiO_2$ substrates for SEM and copper grids for TEM. For each GRM under study, three different samples were investigated collecting images at 9 different locations of each sample. The flake lateral size was also determined by Laser Diffraction (LD) technique in dry state using a Malvern Mastersizer 2000. X-ray Photoelectron Spectroscopy (XPS) analysis was carried out using a ESCAPROBE P (Omnicron) with non-monochromatized MgK radiation (1253.6 eV) spectrometer; the X-ray source operated at 300 W. The residual pressure was lower than $10^{-9}$ Pa during the spectra collection. The binding energy was referenced to the Au 4f 7/2 line at 84.37 eV. X-ray diffraction (XRD) measurements were performed using a Rigaku MiniFlex II at 30 kV and 15 mA, with CuKα radiation, scanning from 3º to 60º with an increment of 0.005º. Sample pellets were used by pressing GRM powders in a 13 mm diameter mould at 5 $Tm/cm^2$. Raman spectra were recorded on a confocal Renishaw inVia Raman microscope at room temperature. The system was equipped with a CCD detector and a holographic notch filter, using excitation wavelength of 532 nm. Scans were acquired from 1000 to 3400 $cm^{-1}$, performing maps of 25 spectra on sample pellets. Spectra analysis and deconvolution were

performed using Wire 4.2 software. The Specific Surface Area (SSA) of GRMs was determined by Brunauer-Emmett-Teller (BET) using an autosorb-6 Quantachrome instruments. The samples were degassed in an autosorb degasser at 250°C for 8h.

## 2.3. Preparation of GRM/PA6 nanocomposites

For the preparation of the concentrated masterbatches, an Alphatech AD30mm LD48 counter rotating twin screw extruder was utilised (Figure 2.a). The GRMs were dispersed in PA6 by melt compounding resulting in concentrated masterbatches. The screw speed was kept at 125 rpm and the feeder speed at 30 rpm. After the preparation of a concentrated masterbatch a dilution step was carried out in a microlaboratory Rondol 10 mm LD20 counter rotating twin screw extruder (Figure 2.b). The process temperature in the different barrels in either extrusion processes are presented in Table 1. The GRM concentration in the diluted samples are shown in Table 2. The GRM's low apparent density (Table 3) limited the maximum achievable % wt in the masterbatches, which was different in every GRM i.e. 15%wt for GNP, 10%wt for GO, 2%wt for rGO and 2.5%wt for f-rGO. This fact was pronounced in the case of rGO and f-rGO fillers, due to their very low apparent density, 2 and 6 g/L, which hindered dossing higher amounts of GRMs within PA6 in the extruder. Also, in the case of GNPs, we observed a decrease in MFI which caused an increase in torque limiting the maximum achievable %wt.

**Figure 2.** Schematic showing the process steps followed for the preparation of the concentrated masterbatches and diluted nanocomposites.

**Table 1.** Barrel temperature profiles used for the GRM/PA6 extrusion in the Alphatech AD30mm and the Rondol 10 mm twin-screw extruders.

| Extruder zones | Z1-Z2 | Z3-Z5 | Z6-Z9 | Z10 |
|---|---|---|---|---|
| | (ºC) | (ºC) | (ºC) | (ºC) |
| Alphatech AD30mm | 190 | 210 | 220 | 230 |
| Rondol 10mm | 170 | 220 | 220 | 230 |

**Table 2.** Concentration of the GRMs in PA6 for masterbatches and diluted nanocomposites.

| GRM | %wt GRM in masterbatch | %wt GRM after dilution |
|---|---|---|
| GNP | 15 | 0.25, 0.5, 1, 3, 5, 7.5, 10 |
| GO | 10 | 1, 3, 5, 7.5 |

| rGO | 2 | 0.1, 0.25, 1 |
| f-rGO | 2.5 | 0.05, 0.15, 0.25, 0.50, 0.75 |

### 2.3.1 Mould preparation for mechanical tests

The extruded composite filaments were pelletised, the granulates were conditioned at 80ºC for 24h and pressure injected in a laboratory injector (AB-100 Plastic Injectors model) at 270ºC with a mould kept at room temperature. The moulds were prepared according to ISO 527-4:1997 [33] and the flexural properties were studied according to ISO 178:2001 [34]. Depending on the mechanical test, and according to the reference standard, tensile or flexural specimens were prepared. At least 5 specimens of each GRM were prepared to ensure reproducibility.

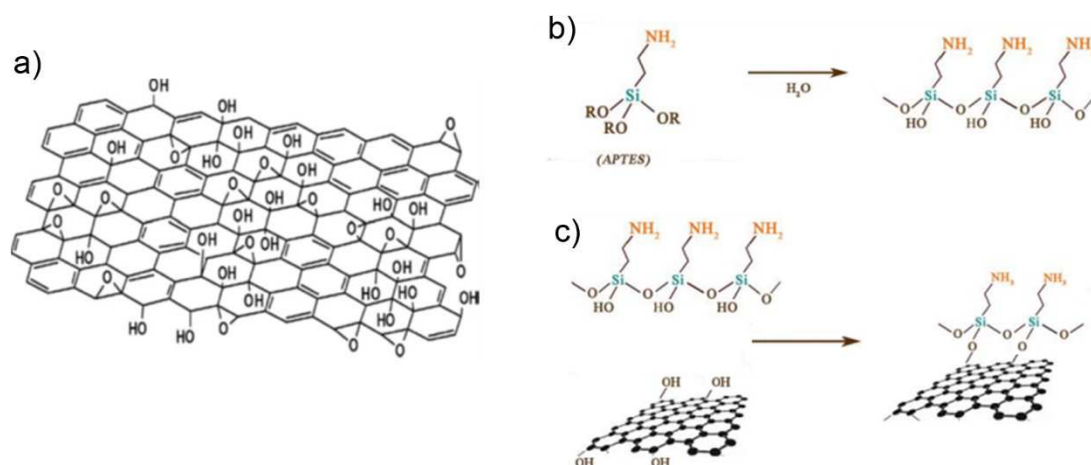### 2.4. Characterisation of GRM/PA6 nanocomposites

The dispersion of the GRMs within the PA6 matrix was studied over cryofractured samples by SEM and SEM/EDX mappings using a Hitachi S-2400 equipped with a Bruker QUANTAX EDS. The MFI expressed in g/10min was determined according to ISO1133 [35] standard using plastometer Mflow, from Zwick Roell. The temperature was set at 235ºC and weight of 2.16 kg (298.2kPa) was applied. The mechanical properties, Young's modulus (E), Ultimate Flexural Strength (UFS), Ultimate Tensile Strength (UTS) and Elongation at break were determined according to ISO 178:2001 [34] for flexure and the ISO 527-4:1997 [33] for tensile using a universal testing machine Shimadzu, AGS-X (10kN). Trapezium X software was used for data acquisition. Tensile tests were performed at constant rate of 10mm/min, while flexural

8

tests were carried out at 2 mm/min. Before mechanical testing, samples were dried at 80ºC for

5 h and conditioned at 23±2ºC and 50±5% of relative humidity for at least 40 h.

## 3. Results and discussion
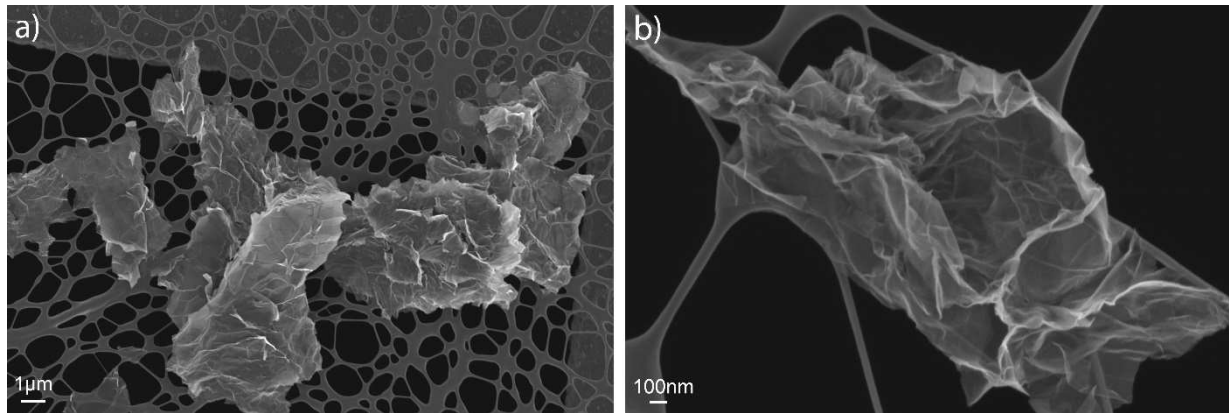
### 3.1. Characterisation of GRMs

Figure 3.a shows the widely accepted chemical structure of GO with hydroxyl (-OH) and

epoxy, groups. Figure 3.b shows the hydrolysis of silane APTES and Figure 3.c shows the

reaction of rGO with silane APTES to form f-rGO.



**Figure 3.** a) Lerf–Klinowski model of GO with the omission of minor groups (carboxyl,

carbonyl, ester, etc.) on the periphery of the carbon plane of the graphitic platelets of GO[36]

[37], b) hydrolysis of silane APTES and c) reaction of rGO with silane APTES to form f-rGO.

Figure 4 shows FESEM images from representative GO and rGO flakes. The lateral size of all

GRM flakes defined as the longest dimension was found, and determined by SEM, to be in the

range of 20-30μm (Table 3). LD measurements gave higher lateral size for all GRMs, in particular in the case of GNPs it was 46±2 μm and for all the rest about 40μm.
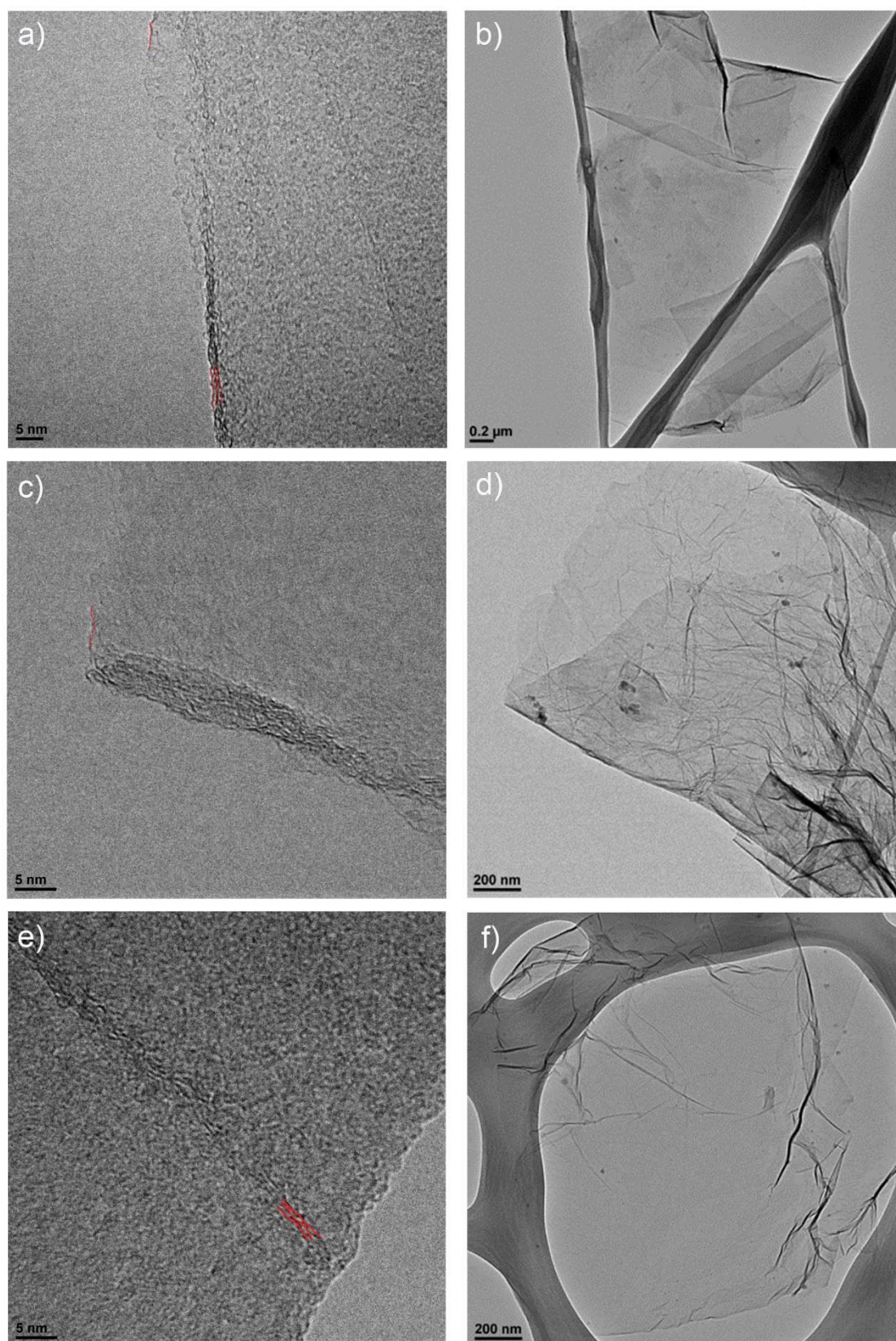


**Figure 4.** FESEM images from representative flakes of a) GO and b) rGO.

The higher lateral size in the case of GNPs could be attributed to the fragmentation of GO, rGO and f-rGO experienced during the oxidation and ultrasonication processes to produce GO [38]. Figure 5 shows TEM imaging of the obtained GO, rGO and f-rGO samples. Samples show a wrinkled structure and low thickness in the range of □1nm; observed in edges of images at high magnifications similar to previously reported graphene materials [39]. SSA values obtained by the BET method are presented in Table 3. The low SSA value ($28 m^2/g$) for GNPs was attributed to incomplete exfoliation of graphite. The GO, rGO and f-rGO showed 435, 512 and 145 $m^2/g$ respectively. According to TEM the number of graphene layers for these GRMs in a stack ($N_G$) is about 3. $N_G$ can be calculated through SSA measured by BET $N_G=2630/SSA$[40] [41] and was found to be 6 for GO, 5 for rGO and 18 for f-rGO. These $N_G$ values obtained via BET for GO, rGO and f-rGO are apparent due to inaccessible surface caused by agglomeration [42], [41]. In the case of f-rGO, the higher $N_G=18$ may be attributed to the final filtration step which causes further agglomeration[41].

**Table 3.** GRM's determined lateral size, thickness, specific surface area (SSA), the number of layer in a stack ($N_G$) and oxygen content.

| GRM | Lateral size by SEM (μm) | Lateral size by LD D50 (μm) | Thickness by TEM (nm) | SSA ($m^2$/g) | XPS (%O) | Apparent density (g/L) |
|---|---|---|---|---|---|---|
| GNP | 20-30 | 46±2 | - | 28 | <1 | 72 |
| GO | 20-30 | 39±2 | □1 | 435 | 31 | 48 |
| rGO | 20-30 | 41±2 | □1 | 512 | 6.05 | 2 |
| f-rGO | 20-30 | 38±2 | □1 | 145 | 6.8 (0.4 Si) | 6 |

**Figure 5.** TEM images obtained from typical flakes of a-b) GO, c-d) rGO and e-f) f-rGO.
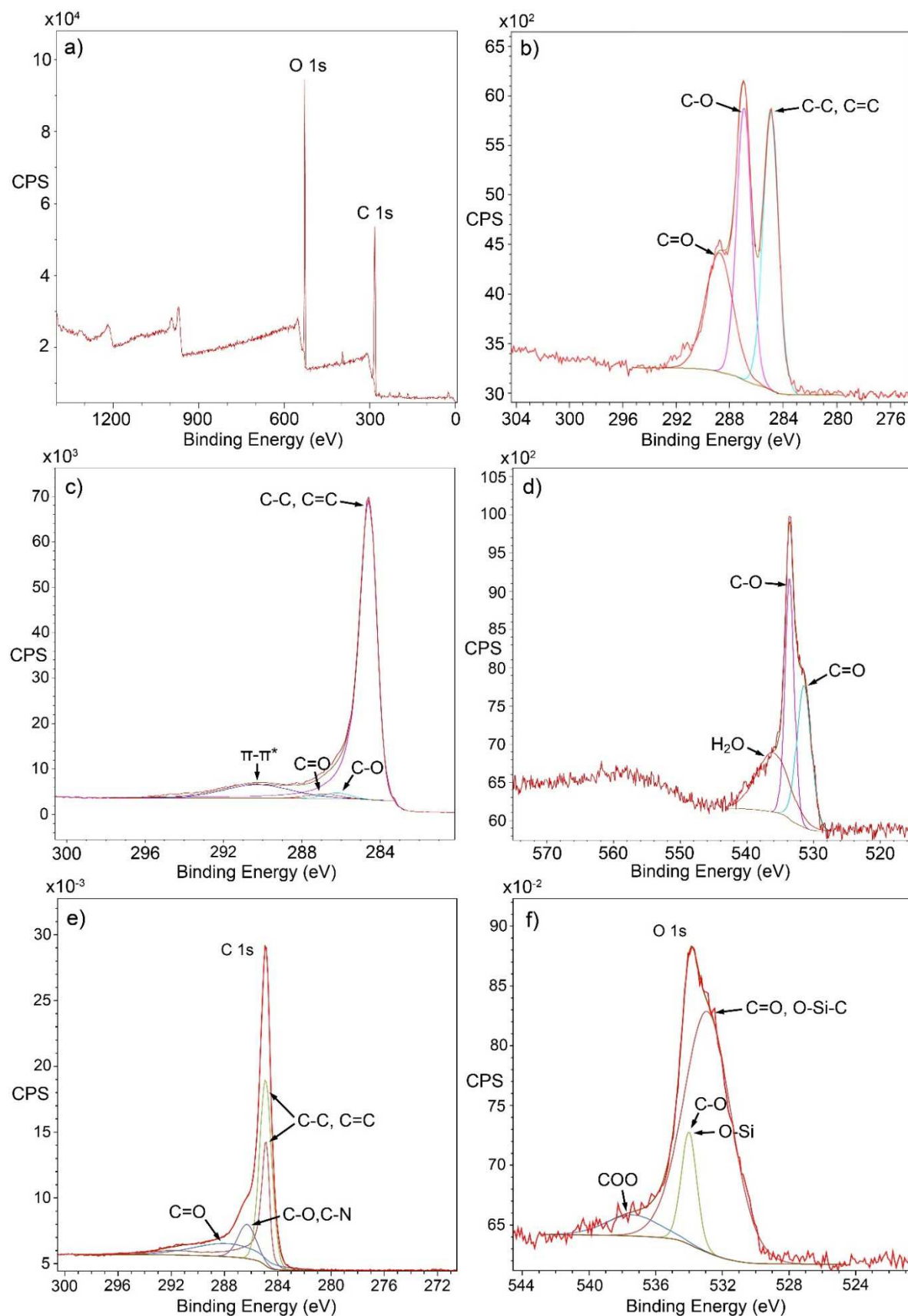
XPS was utilised to determine the oxygen content of the prepared GRMs. Spectra of $O_{1s}$ and $C_{1s}$ peaks for GO are presented in Figure 6 (a-b). Deconvoluted $C_{1s}$ (left) and $O_{1s}$ (right) peaks for rGO are given in Figure 6 (c-d) and deconvoluted peaks of f-rGO are given in Figure 6 (e-f). The deconvolution of XPS spectra have shown the presence of different content of oxygen (Table 3) in various functional groups. Deconvolution of $C_{1s}$ peak of GO reveals the existence of three components with similar intensity: C=O (288.8eV, 27.9%), C-O (at 286.9 eV and 35.3% of total) and C=C and C-C links (at 284.9 eV and 36.8% of intensity).

The deconvolution of $C_{1s}$ peak of rGO has shown that the majority of oxygen is in alkoxy and ether form (286.58 eV, 5.18% of C-O) and carbonyl bonds C=O (288.84 eV, 1.72%). There is a contribution of aromaticity (291.13 eV, 6.65%); the oxygen content is significantly smaller than that in case of GO.
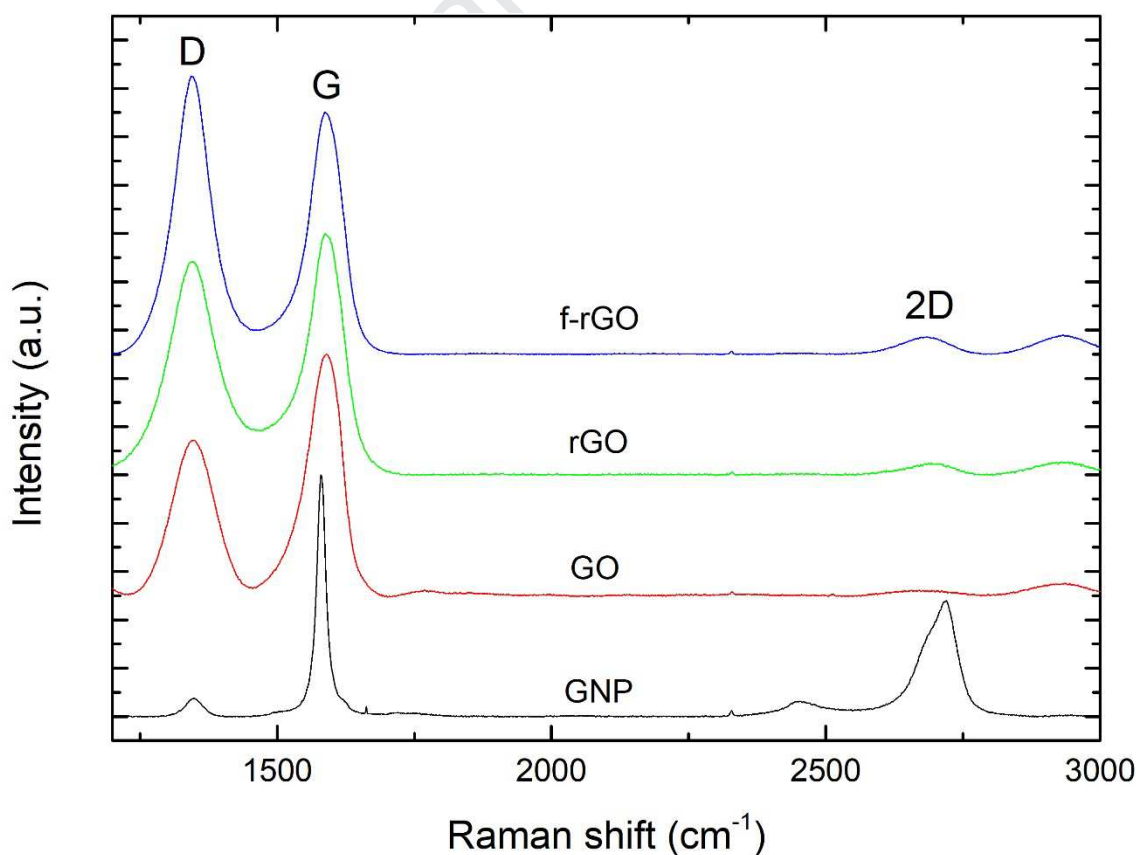
For f-rGO the N peak, which could come from amino group -$NH_2$ in APTES, is not observed in XPS spectra. However, a Si band appears at $\sim$103 eV, with an intensity of 0.4%. Oxygen content is 6.8%, and C contents has been determined at 92.2%. Deconvolution of $C_{1s}$ peak shows C=O bonds (in 287.8 eV, 16.5%), C-O and/or C-N at 286.3 eV (11.5%); and peaks for carbon double and simple bonds, C=C and C-C (71%). The $O_{1s}$ peak shows three components with the following binding energies: 532.9 eV (79.9%, due to C=O and O-Si-C), 534 eV (12.3% and related to C-O and/or O-Si) and 537.4 eV (7.8%, due to COO groups).

As expected, GO shows the highest oxygen percentage (30.7%). The oxygen content follows the order GO > f-rGO > rGO > GNP. The majority of the oxygen is in alkoxy form (C-O) with little contribution of aromaticity. However, the asymmetry of the carbon peak indicates the presence of oxygen on the surface. The concentration of carboxylic groups -COOH is very small.

**Figure 6.** a) XPS spectra of GO, b) $C_{1s}$ deconvoluted peak, c-d) deconvoluted $C_{1s}$ and $O_{1s}$ peaks of rGO, e-f) $C_{1s}$ and $O_{1s}$ deconvoluted peaks of f-rGO.

14

Raman spectra obtained from the GRMs under study are shown in Figure 7. The Raman spectrum of GNP flakes shows a small D peak at 1349cm$^{-1}$, and an intense G peak at 1580cm$^{-1}$ with an intensity ratio of the D to G peaks $I_D/I_G$=0.08 and a 2D peak at 2718 cm$^{-1}$ and $I_{2D}/I_G$ = 0,48 (Table 4). The rest of the GRMs show an intense D peak present at $\sim$1350 cm$^{-1}$ in all samples, which confirms the lattice distortions[43]. Also a G peak positioned at 1588 cm$^{-1}$ for the rGO and at 1563 cm$^{-1}$ for the GO, corresponding to the superposition of 2 peaks; the first-order scattering of the $E_{2g}$ mode of G and the contribution of D′ band[44]. The increase of the $I_D/I_G$ ratio from GO to rGO after the thermochemical reduction has been previously reported [45],[30]. $I_D/I_G$ for f-rGO is higher than that observed for rGO, indicating higher concentration of defects for the f-rGO**Error! Bookmark not defined.**. GO, rGO and f-rGO shows a low intensity 2D band and very small $I_{2D}/I_G$ ratio from 0.05 to 0.08.
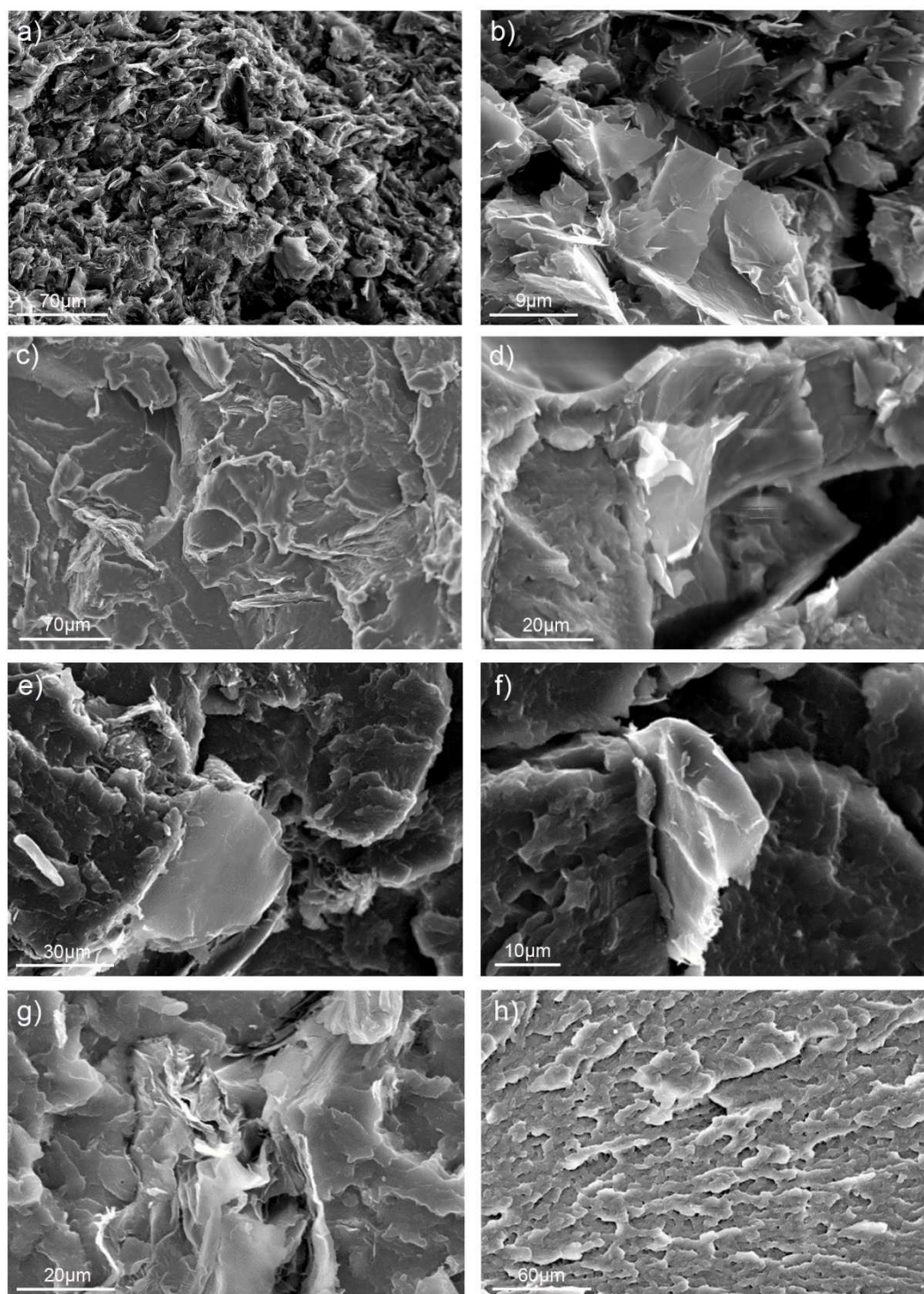
**Figure 7**. Representative RAMAN spectra of GRMs studied.

**Table 4.** Characteristic Raman peaks and intensity ratios for the GRMs under study.

| GRM | D (cm$^{-1}$) | G (cm$^{-1}$) | 2D (cm$^{-1}$) | $I_D/I_G$ | $I_{2D}/I_G$ |
|-----|-----|-----|-----|-----|-----|
| GNP | 1349 | 1580 | 2718 | 0.08 | 0.48 |
| GO | 1347 | 1563 | 2674 | 0.66 | 0.05 |
| rGO | 1349 | 1588 | 2691 | 0.88 | 0.05 |
| f-rGO | 1345 | 1588 | 2680 | 1.17 | 0.08 |

### 3.2. Microscopical investigation of GRM/PA6 nanocomposites

The dispersion of the GRMs within the PA6 matrix was studied by SEM. Images of cryo-fractured of GRM/PA6 samples are shown in Figure 8(a-h). GNP/PA6 samples containing 15%wt GNPs (Figure 8a) show areas with low GNP content and areas with large aggregates of GNPs with lateral size over 100 μm and thickness up to 10 μm, indicating a weak interaction between the matrix and the filler. Discrete wrinkled GNP particles and lower agglomeration can be observed in Figure 8.b at 1% of loading, as a result of the second extrusion process. The different surface chemistry and morphology (lower thickness and wrinkled structure) of GO, rGO and f-rGO caused differences in dispersion and agglomeration of GRM particles. The SEM image in Figure 8c, taken from the concentrated masterbatch (10%wt) of GO, show large aggregates of 70 μm and thickness about 7-10 μm (Figure 8c). However, when the masterbatch is diluted through a second melt compounding process to obtain final formulations, the presence of large aggregates is drastically reduced. This effect has also been observed by other authors[46]. No large particles or aggregates were observed in Figure 8d (1%wt GO).
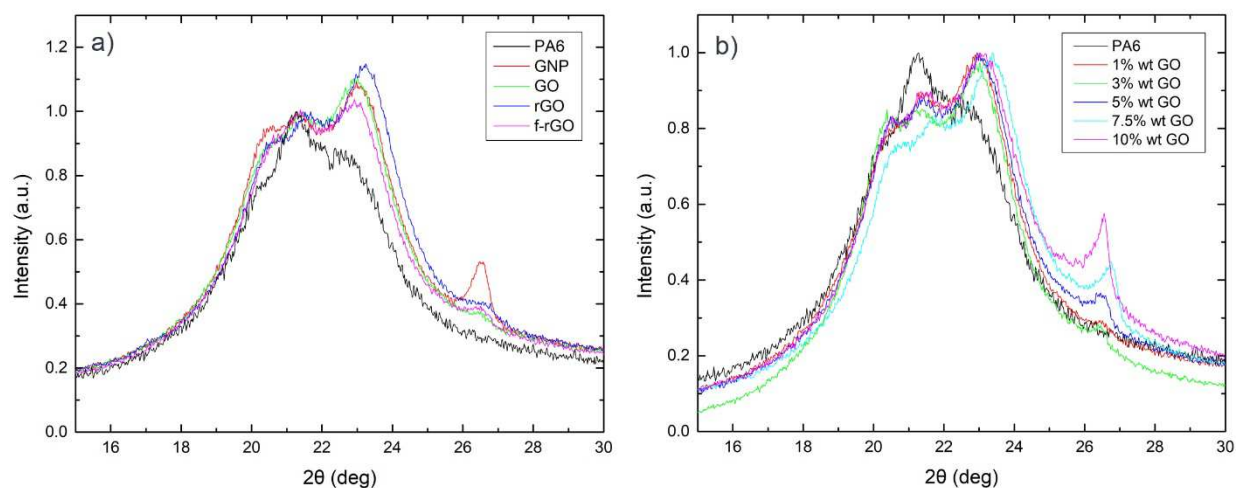
**Figure 8.** SEM micrographs of a) 15%wt GNP masterbatch b) 1%wt GNP, c) 10%wt GO masterbatch d) 1%wt GO, e) 2%wt rGO masterbatch f) 1%wt rGO, g) 2.5%wt f-rGO masterbatch and h) 0.05%wt f-rGO.

SEM images obtained from rGO masterbatch (2%wt) in Figure 8e shows aggregation with more than 40 μm in lateral size and about 3 μm in thickness. After the second extrusion samples with 1%wt rGO showed decreased aggregation maintaining though the lateral flake size (~40 μm). In the case of f-rGO, the masterbatch (2.5%wt) showed some agglomerates (Figure 8.g); but in less quantity than the masterbatch of GO. The presence of 30 μm sheets with less than 1 μm thickness can be identified. This can be attributed to better dispersion, due to an increase in the compatibility because of silane functionalization. A good dispersion was finally observed in the diluted 0.05%wt f-rGO/PA6 samples shown in Figure 8.h.

## 3.3. Crystallinity

X-ray diffractograms obtained from PA6 and GRM/PA6 samples are presented in Figure 9(a-b). All samples showed the $\alpha_1$ (200), $\alpha_2$ (002/202) and $\gamma_2$ (011) phases of PA6 [47]. XRD spectras obtained from GRM/PA6 nanocomposites containing 1%wt filler (Figure 9.a) revealed an increase in $\alpha_1$ phase ($2\theta \Box 20.3°$) and in $\alpha_2$ phase ($2\theta \Box 23°$) and a decrease of $\gamma_2$ phase ($2\theta \Box 21.4°$), in respect to neat PA6 [47]. Previous analysis in neat PA6 revealed that conversion of $\gamma$ phase into $\alpha$ phase results in improvements in E and UTS due to reduction of the distance between polymer chains [48], [49]. For GNP/PA6 the (002) peak of graphite at $2\theta=26.54°$ was clearly observed due higher flake thickness. Figure 9b shows the XRD diffraction patterns of GO/PA6 nanocomposites (up to 10%wt). An increase in the $\alpha_1$ and $\alpha_2$ and a decrease in the $\gamma_2$ is observed with the addition of GO. The in-situ reduction of GO, during the melt compounding process, is in accordance to previous studies [50], [51]. The (002) peak from the graphitic phase is only observed at high GO loadings over 5%wt.
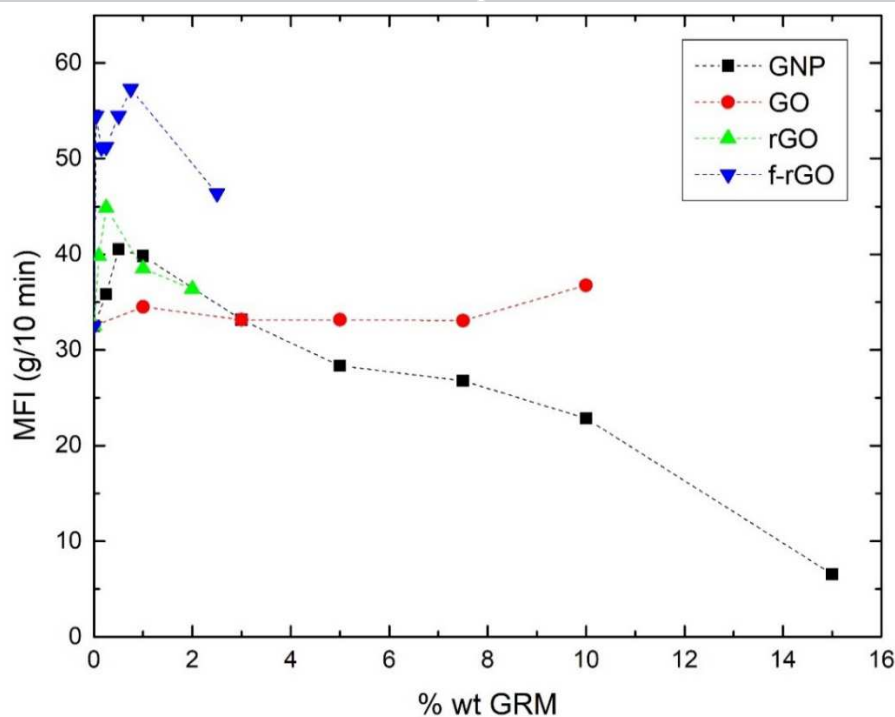
18

**Figure 9.** X-ray diffractograms of a) neat PA6 and 1%wt GRMs in PA6 and b) neat PA6 and different %wt of GO (1-10%wt).

## 3.4. Melt flow index

The incorporation of fillers into a polymer matrix usually reduces the mobility of the polymer chains and increases viscosity thus making the melt difficult to process [29]. The MFI being inversely proportional to viscosity[52]; is a measure of the ability of the material's melt to flow under pressure. Figure 10 show the MFI of the GRM/PA6 nanocomposites under study. The MFI is highly dependent on the type and the %wt of GRM filler. In the case of GNP/PA6, the MFI increases at low loadings, peaks at 40 g/10min for 0.5%wt and then drastically decreases at higher filler content. The increase in MFI at low loadings can be attributed to a lubricant effect of the GNPs, however, higher quantity of nanoparticles leads to viscosity increase and thus a reduction in MFI of 80% compared with the neat PA6 resin. This result is similar to previous reports for expanded graphite composites where an increased flowability at low loadings and increased viscosity at higher loadings were observed [53]. The MFI for GO is independent of the %wt GRM. It is important to mention that the GO has been reduced to rGO during the extrusion process as observed by XRD. rGO/PA6 nanocomposites shown

enhancements up to 10% in MFI; having a lubricant effect more pronounced than GO but smaller than f-rGO. The increase in MFI observed for rGO, f-rGO and GO nanocomposites can be attributed to the change in the intensity of the crystalline phases $\alpha$ and $\gamma$ of PA6 (Figure 9). Lowering of the $\gamma$ crystalline phase has been correlated with an increase in the mobility of the polymer chains in SWCNTs/PA6 [54] and montmorillonite/PA6 nanocomposites [55]. It is important to mention that this material does not reduce the flow of the polymer; which is a key parameter in industrial processes. More than 70% of enhancement has been determined in MFI in all the nanocomposites containing f-rGO; with the maximum being 76.5% at 0.75%wt. This pronounced change can be due to the plasticising effect that functionalized graphene can produce. Better dispersion and interface between polymer and functionalized graphene has been observed by SEM micrographs, compared to GO or rGO sheets; less aggregation can be responsible for high MFI. Similar effect was observed previously in talk functionalised with APTES, which showed an increase in the MFI compared to unfunctionalised one [56]. Also, in nanoclay/PA11 nanocomposites, at low loadings (2%), the APTES modified nanocomposite exhibited lower increase in viscosity compared to the unfunctionalized [57].
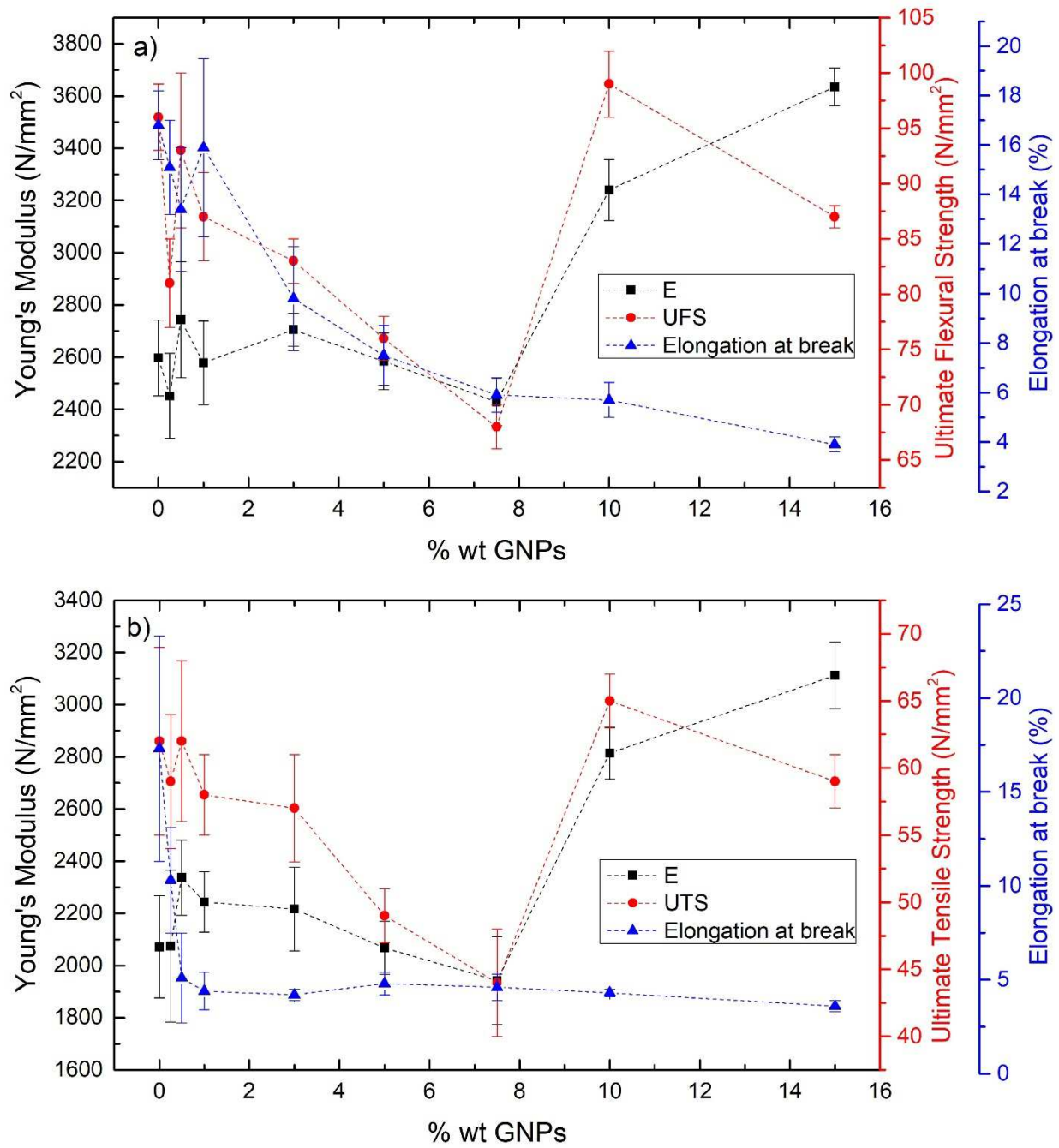
**Figure 10.** MFI of RGM/PA6 nanocomposites as a function of %wt for different GRM.

### 3.5. Mechanical properties of GRM/PA6 nanocomposites

*3.5.1 GNP/PA6*

The mechanical properties, E, UFS, UTS, elongation at break of the masterbatches and diluted nanocomposites have been determined by flexural and tensile tests. Flexural tests of GNP/PA6 nanocomposites revealed a significant increase of E from $2597\pm145$ N/mm$^2$ of neat PA6 to $3240\pm117$ N/mm$^2$ and $3635\pm72$ N/mm$^2$ at 10%wt and 15%wt GNP respectively (Figure 11a). A significant decrease in elongation at break is observed with increasing GNP loading, from 16.8% (neat PA6) to 3.9% for 15%wt loading. About 50% increase was observed in E in tensile tests (Figure 11b). The elongation at break decreased more than 75%, revealing that the nanocomposite became more rigid.
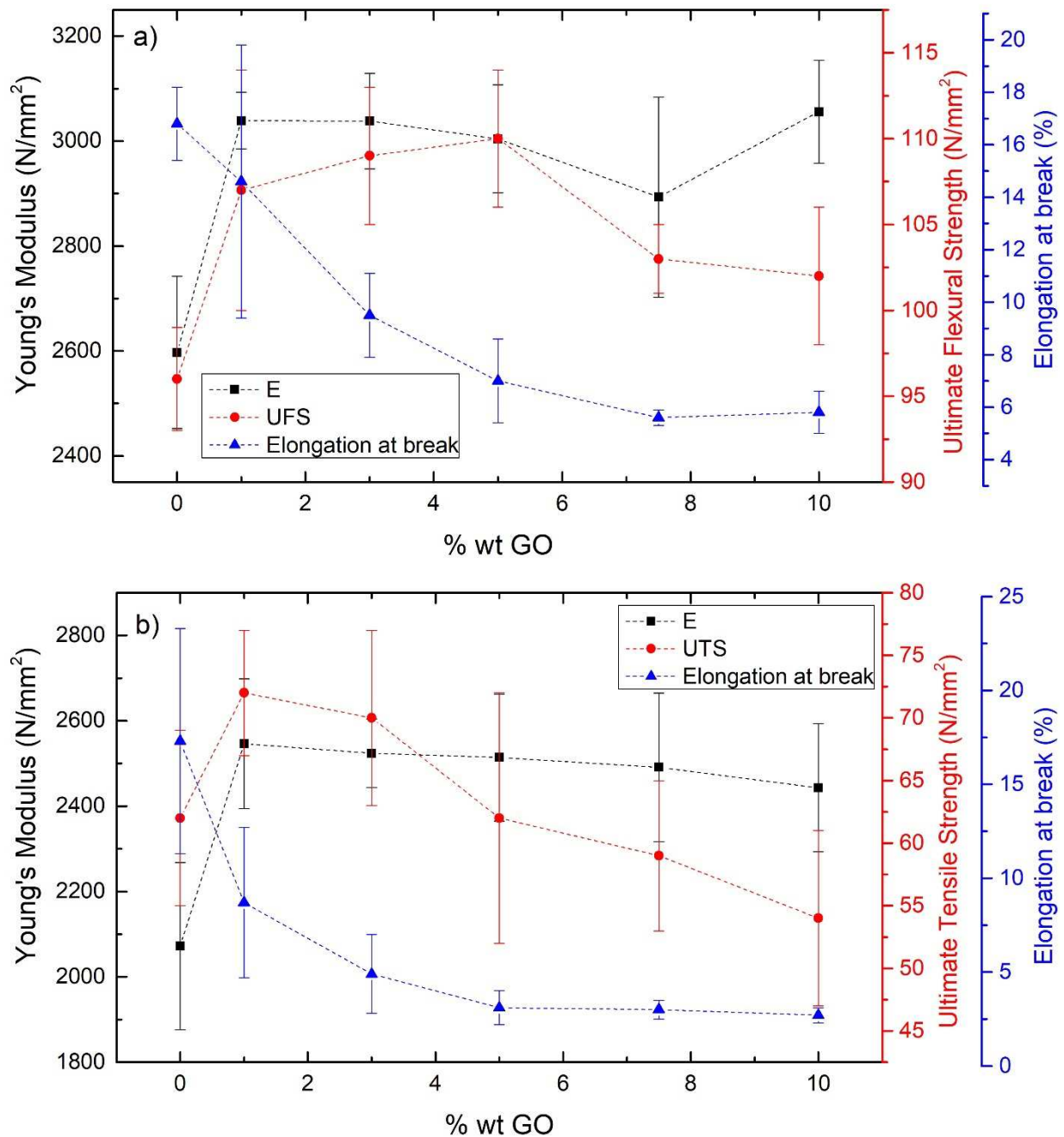
**Figure 11.** Results obtained by a) flexural and b) tensile tests on GNP/PA6 nanocomposites.

*3.5.2 GO/PA6*

In flexural, tests, all GO/PA6 formulations from 1 to 10%wt showed similar improvements in

E and UFS with values of □3000 N/mm$^2$ and 105 N/mm$^2$ respectively (Figure 12a). However,

a pronounced reduction was observed in elongation at break from 16.8% to 5.6% at 7.5%wt

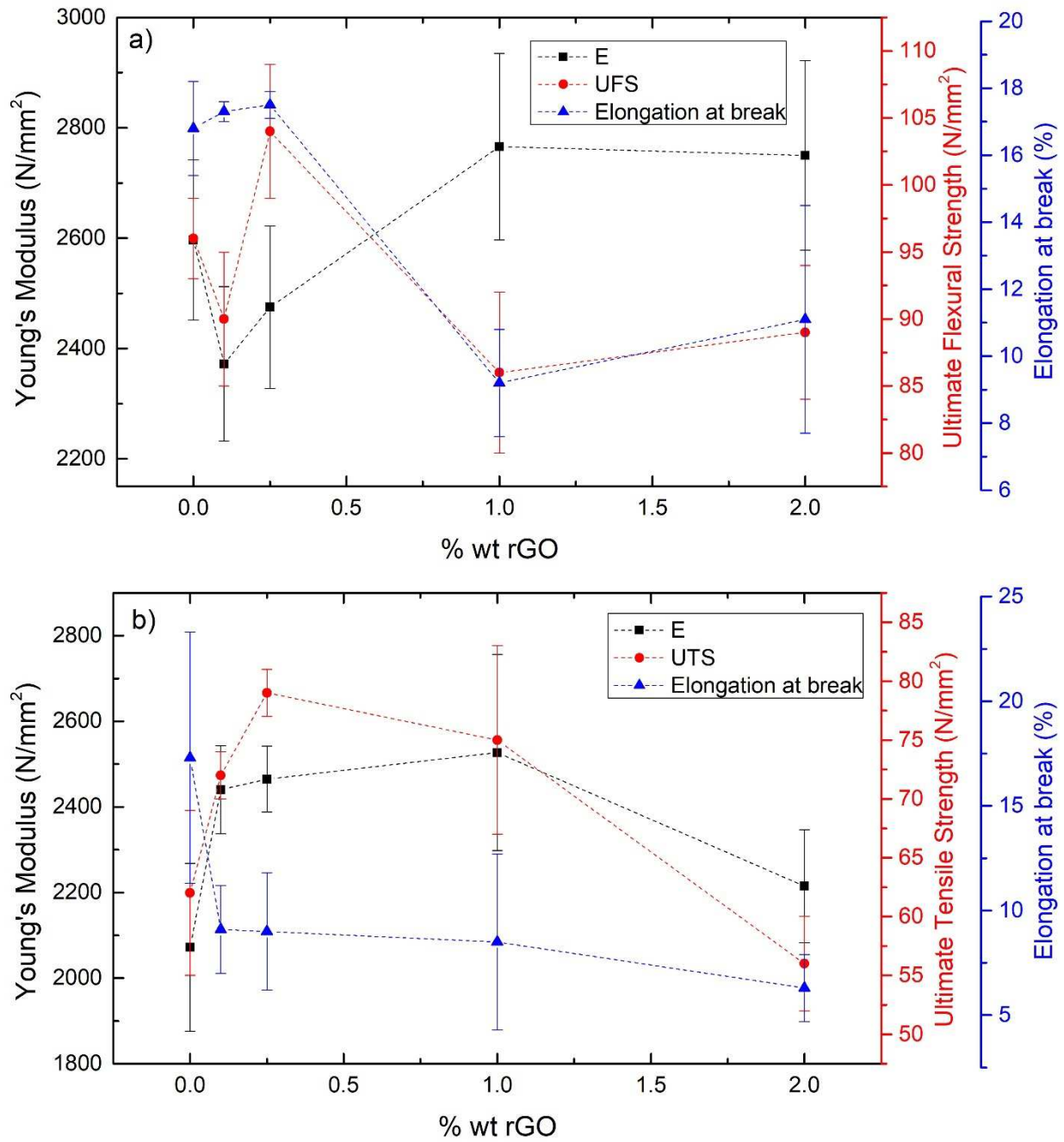GO which is similar to 10%wt loading. In tensile (Figure 12b), all formulations (1-10%wt GO) presented an increase of ☐20% in E in respect to neat PA6. Lower GO content (1% and 3%wt) also increase UTS. A significant reduction in elongation was observed at break from 17.3% to 3.1% at 5%wt loading and kept constant up to 10%wt.



**Figure 12.** Results obtained by a) flexural and b) tensile tests on GO/PA6 nanocomposites.

*3.5.3 rGO/PA6*

Under flexural tests, rGO/PA6 nanocomposites do not presented significant improvements in E and UFS (Figure 13a) which can be attributed to the lower content of polar groups of rGO leading to lower interaction with the polymer chains. The elongation at break reduces from 16.8% for the PA6 to 9.2% for 1%wt loading. In tensile (Figure 13b), rGO/PA6 nanocomposites show an increase in E up to a maximum value of $2527\pm229$ N/mm$^2$ for 1%wt and a maximum UTS of $79\pm2$ N/mm$^2$ for 0.25%wt. The elongation at break reduces from 17.3% for the PA6 to 6.3% for 2%wt rGO.

**Figure 13.** Results obtained by a) flexural and b) tensile tests on rGO/PA6 nanocomposites.

*3.5.4 f-rGO/PA6*

In flexural tests the addition of f-rGO in PA6 did not cause any significant change in E (Figure 14a). A significant increase in UFS was observed from 96 N/mm² in the neat PA6 to 118 N/mm² in the masterbatch (2.5%wt f-rGO). A decrease in elongation at break from 16.8±1.4 to

25

$11.1\pm2.0$ was also observed in the 2.5%wt f-rGO formulation. In tensile tests (Figure 14b), both E and UTS increased considerably with the addition of f-rGO and presented a maximum of $2877\pm185$ N/mm$^2$ and $86\pm3$ N/mm$^2$ respectively at 0.5%wt loading. On the contrary, the elongation at break decreases from $17.3\pm6.0$ to $4.2\pm0.4$ at 2.5%wt loading.


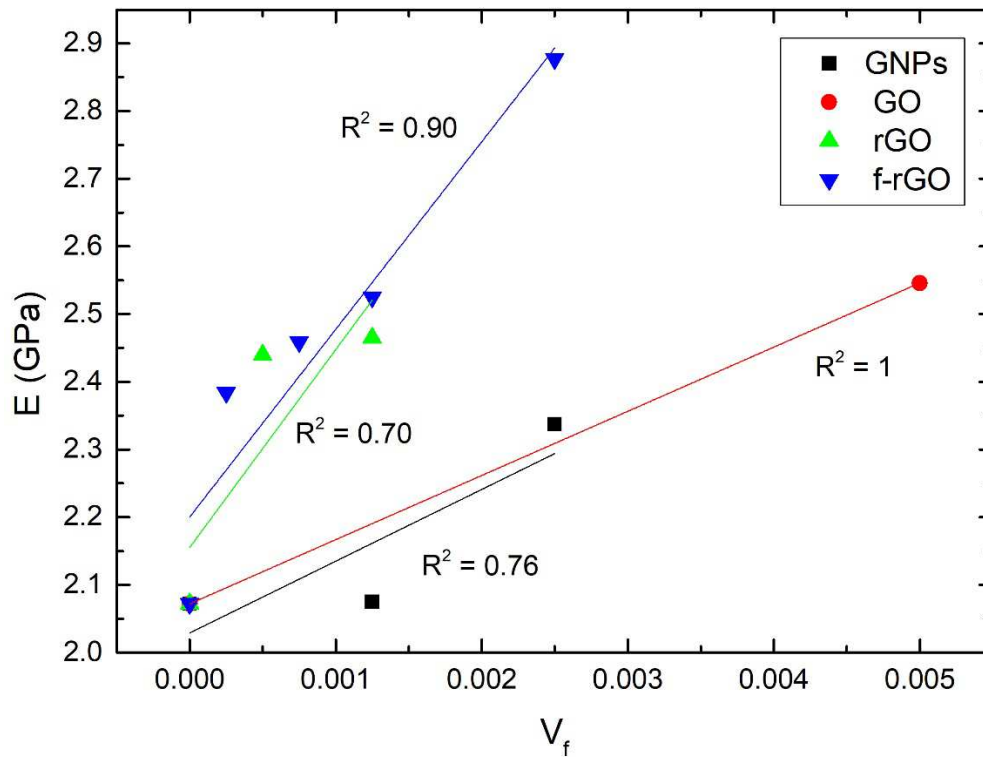
**Figure 14.** Results obtained by a) flexural and b) tensile tests on f-rGO/PA6 nanocomposites.

It is remarkable that f-rGO nanocomposites showed at very low loadings a simultaneous increase in UTS and elongation at break, and at moderate loadings considerable increase in UTS without significant reduction in elongation at break. Similar results were also observed by Wang et al. [58] in other GRM/PA6 nanocomposites at very low loadings (≤1% wt of functionalised $MoS_2$ nanosheets), and improvements were attributed to good dispersion of the nanofiller and strong interfacial interaction between the nanofiller and the polymer matrix. Superior mechanical properties were observed in functionalised $MoS_2$/PA6 nanocomposites compared to those containing unfunctionalized $MoS_2$, which was attributed to higher capacity of transferring the stress from the PA6 matrix to the functionalised nanosheets. Similar interfacial effects have been observed in exfoliated nanoclays in polyamide matrix [59]; showing improved mechanical properties over the non-exfoliated material. Brittle to ductile transition can be also have effect in the observed increase in elongation at break and UTS in the f-rGO at very low loadings [60]. The standard deviation observed is in agreement with dense and sparse zones remarkable at very low loadings [61]. The optimum reinforcement in the case of f-rGO, was obtained at 0.5%wt. Higher loading deteriorate mechanical properties due to the formation of agglomerates and restacking [62]. In the case of rGO, the optimum reinforcement was achieved at lower loadings, probably due to higher agglomeration as observed by SEM. Figure 15 shows E as a function of the volume fraction of GRMs. We applied the rule of mixtures to calculate the Effective Modulus of the GRMs [63] [64][65]

$$E = E_{eff}V_f + E_mV_m$$

where $E$, $E_{eff}$, $E_m$ are the Young's Modulus of the nanocomposite, the filler and matrix respectively, and $V_f$ and $V_f$ are the volume fractions of the GRM filler and the matrix respectively (with $V_f + V_m = 1$). The $E_{eff}$ of GNPs, GO, rGO and f-rGO were calculated to be 106, 95, 292 and 277 GPa respectively. This is no far from theoretically predicted values for GNPs (~350 GPa for 10 atomic layers [63].

27

**Figure 15.** Variation of the Young's Modulus with volume fraction of the filler.

## 4. Conclusions

In this work, GRM/PA6 nanocomposites were prepared by melt compounding using a two-phase twin screw extrusion process. In the first extrusion phase we were able to prepare masterbatches with a maximum GRM loading of 15, 10, 2 and 2.5%wt for GNP, GO, rGO and f-rGO respectively. A second extrusion phase produced formulations with lower concentration promoting the dispersion of the GRMs in the PA6 matrix. All prepared nanocomposites showed a sharp increase in MFI which was peaked around 0.5-1%wt, due to their lubricant effect which enhanced processability. Remarkable was the increase in MFI of over 76% with the addition of 0.5 %wt f-rGO, which was attributed to enhanced interface interaction between the matrix and the nanofiller, higher than that observed in unfunctionalized rGO. In terms of

28

mechanical properties, all GRM/PA6 nanocomposites showed improvements in E and UTS and UFS compared to neat polymer. GNPs/PA6 nanocomposites showed the highest improvement in E of 50% at a high loading of 15%wt. In the case of f-rGO/PA6, both E and UTS increased by 39% at low loading of 0.5%wt. Using the rule of mixtures, it was found that the Effective Modulus of rGO (292 GPa) and f-rGO (277 GPa) flakes are much higher than that of GNPs (106 GPa) and GO (95 GPa).

**Acknowledgements**

**References**

[1]    Y. Kojima *et al.*, "Novel preferred orientation in injection☐molded nylon 6☐clay hybrid," *J. Polym. Sci. Part B Polym. Phys.*, 1995, doi: 10.1002/polb.1995.090330707.

[2]    B. Gupta, M. F. Lacrampe, and P. Krawczak, "Polyamide-6/clay nanocomposites: A critical review," *Polymers and Polymer Composites*. 2006.

[3]    N. Štrumberger, A. Gospočić, M. Hvu, and Č. Bartulić, "Polymeric materials in automobiles," *Promet - Traffic - Traffico*, 2005.

[4]    J. G. Lim, B. S. Gupta, and W. George, "The potential for high performance fiber from nylon 6," *Progress in Polymer Science*. 1989, doi: 10.1016/0079-6700(89)90009-9.

[5]    B. Aldousiri, A. Shalwan, and C. W. Chin, "A review on tribological behaviour of polymeric composites and future reinforcements," *Adv. Mater. Sci. Eng.*, 2013, doi: 10.1155/2013/645923.

[6]   M. F. Maitz, "Applications of synthetic polymers in clinical medicine," *Biosurface and Biotribology*, 2015, doi: 10.1016/j.bsbt.2015.08.002.

[7]   S. Pan and Z. Zhang, "Fundamental theories and basic principles of triboelectric effect: A review," *Friction*. 2019, doi: 10.1007/s40544-018-0217-7.

[8]   J. W. Cho and D. R. Paul, "Nylon 6 nanocomposites by melt compounding," *Polymer (Guildf).*, vol. 42, pp. 1083–1094, 2001, doi: 10.1016/S0032-3861(00)00380-3.

[9]   M. K. Akkapeddi, "Glass fiber reinforced polyamide-6 nanocomposites," *Polym. Compos.*, 2000, doi: 10.1002/pc.10213.

[10]  H. Unal, F. Findik, and A. Mimaroglu, "Mechanical behavior of nylon composites containing talc and kaolin," *J. Appl. Polym. Sci.*, 2003, doi: 10.1002/app.11927.

[11]  M. Avella, M. E. Errico, and G. Gentile, "Nylon 6/calcium carbonate nanocomposites: Characterization and properties," *Macromol. Symp.*, 2006, doi: 10.1002/masy.200650222.

[12]  S. Sinha Ray and M. Okamoto, "Polymer/layered silicate nanocomposites: A review from preparation to processing," *Progress in Polymer Science (Oxford)*. 2003, doi: 10.1016/j.progpolymsci.2003.08.002.

[13]  J. H. Lin *et al.*, "Using multiple melt blending to improve the dispersion of montmorillonite in polyamide 6 nanocomposites," *Polym. Test.*, 2016, doi: 10.1016/j.polymertesting.2016.09.016.

[14]  T. D. Fornes, D. L. Hunter, and D. R. Paul, "Effect of sodium montmorillonite source on nylon 6/clay nanocomposites," *Polymer (Guildf).*, 2004, doi: 10.1016/j.polymer.2004.01.061.

[15]  G. Srinath and R. Gnanamoorthy, "Effect of organoclay addition on the two-body abrasive wear characteristics of polyamide 6 nanocomposites," *J. Mater. Sci.*, 2007, doi: 10.1007/s10853-006-0165-x.

[16]  Z. Shen, S. Bateman, D. Y. Wu, P. McMahon, M. Dell'Olio, and J. Gotama, "The effects of carbon nanotubes on mechanical and thermal properties of woven glass fibre reinforced polyamide-6 nanocomposites," *Compos. Sci. Technol.*, 2009, doi: 10.1016/j.compscitech.2008.10.017.

[17]  T. Kuilla, S. Bhadra, D. Yao, N. H. Kim, S. Bose, and J. H. Lee, "Recent advances in graphene based polymer composites," *Prog. Polym. Sci.*, 2010, doi: 10.1016/j.progpolymsci.2010.07.005.

[18]  R. Verdejo, M. M. Bernal, L. J. Romasanta, and M. a. Lopez-Manchado, "Graphene filled polymer nanocomposites," *J. Mater. Chem.*, vol. 21, no. 10, pp. 3301–3310, 2011, doi: 10.1039/c0jm02708a.

[19]  R. Shah, A. Kausar, B. Muhammad, and S. Shah, "Progression from Graphene and Graphene Oxide to High Performance Polymer-Based Nanocomposite: A Review," *Polym. - Plast. Technol. Eng.*, 2015, doi: 10.1080/03602559.2014.955202.

[20]  H. Kim, A. A. Abdala, and C. W. Macosko, "Graphene/Polymer Nanocomposites," *Macromolecules*, vol. 43, pp. 6515–6530, 2010.

[21]  X. Fu, C. Yao, and G. Yang, "Recent advances in graphene/polyamide 6 composites: a review," *RSC Adv.*, vol. 5, no. 76, pp. 61688–61702, 2015, doi: 10.1039/C5RA09312K.

[22]  W. Liu, I.-H. Do, H. Fukushima, and L. T. Drzal, "Influence of Processing on Morphology, Electrical Conductivity and Flexural Properties of Exfoliated Graphite

Nanoplatelets-Polyamide Nanocomposites," *Carbon Lett.*, vol. 11, no. 4, pp. 279–284, 2010, doi: 10.5714/CL.2010.11.4.279.

[23] P. Steurer, R. Wissert, R. Thomann, and R. M??lhaupt, "Functionalized graphenes and thermoplastic nanocomposites based upon expanded graphite oxide," *Macromol. Rapid Commun.*, vol. 30, no. 4–5, pp. 316–327, 2009, doi: 10.1002/marc.200800754.

[24] K. Scully and R. Bissessur, "Decomposition kinetics of nylon-6/graphite and nylon-6/graphite oxide composites," *Thermochim. Acta*, vol. 490, no. 1–2, pp. 32–36, 2009, doi: 10.1016/j.tca.2009.01.029.

[25] Z. Xu and C. Gao, "In situ polymerization approach to graphene-reinforced nylon-6 composites," *Macromolecules*, vol. 43, no. 16, pp. 6716–6723, 2010, doi: 10.1021/ma1009337.

[26] N. Du, C. yue Zhao, Q. Chen, G. Wu, and R. Lu, "Preparation and characterization of nylon 6/graphite composite," *Mater. Chem. Phys.*, vol. 120, no. 1, pp. 167–171, 2010, doi: 10.1016/j.matchemphys.2009.10.041.

[27] J. Zhong, A. I. Isayev, and X. Zhang, "Ultrasonic twin screw compounding of polypropylene with carbon nanotubes, graphene nanoplates and carbon black," *Eur. Polym. J.*, 2016, doi: 10.1016/j.eurpolymj.2016.04.028.

[28] H. Fukushima, L. T. Drzal, and E. L. Mi, "Nylon - Exfoliated Graphite Nanoplatelet ( xGnP ) Nanocomposites with Enhanced Mechanical , Electrical and Thermal Properties," *NSTI-Nanotech*, 2006.

[29] B. Mayoral *et al.*, "Melt processing and characterisation of polyamide 6/graphene nanoplatelet composites," *RSC Adv.*, vol. 5, no. 65, pp. 52395–52409, 2015, doi:

10.1039/C5RA08509H.

[30]  S. Colonna, O. Monticelli, J. Gomez, C. Novara, G. Saracco, and A. Fina, "Effect of morphology and defectiveness of graphene-related materials on the electrical and thermal conductivity of their polymer nanocomposites," *Polym. (United Kingdom)*, 2016, doi: 10.1016/j.polymer.2016.09.032.

[31]  W. S. Hummers and R. E. Offeman, "Preparation of Graphitic Oxide," *J. Am. Chem. Soc.*, 1958, doi: 10.1021/ja01539a017.

[32]  J. Gómez, E. Villaro, A. Navas, and I. Recio, "Testing the influence of the temperature, RH and filler type and content on the universal power law for new reduced graphene oxide TPU composites," *Mater. Res. Express*, 2017, doi: 10.1088/2053-1591/aa8e11.

[33]  "ISO 527-4:1997 - Plastics — Determination of tensile properties — Part 4: Test conditions for isotropic and orthotropic fibre-reinforced plastic composites."

[34]  "ISO 178:2001 - Plastics — Determination of flexural properties."

[35]  "ISO 1133-1:2011 - Plastics — Determination of the melt mass-flow rate (MFR) and melt volume-flow rate (MVR) of thermoplastics — Part 1: Standard method."

[36]  A. Lerf, H. He, M. Forster, and J. Klinowski, "Structure of Graphite Oxide Revisited ‖," *J. Phys. Chem. B*, vol. 102, no. 23, pp. 4477–4482, 1998, doi: 10.1021/jp9731821.

[37]  J. Klinowski, A. Lerf, H. He, and M. Forster, "A new structural model for graphite oxide," *Chem. Phys. Lett.*, 1998, doi: 10.1016/S0009-2614(98)00144-4.

[38]  S. Y. Chee, H. L. Poh, C. K. Chua, F. Šaněk, Z. Sofer, and M. Pumera, "Influence of parent graphite particle size on the electrochemistry of thermally reduced graphene oxide," *Phys. Chem. Chem. Phys.*, 2012, doi: 10.1039/c2cp41462g.

[39] D. Golberg *et al.*, "Nanomaterial engineering and property studies in a transmission electron microscope," *Adv. Mater.*, 2012, doi: 10.1002/adma.201102579.

[40] S. Gadipelli and Z. X. Guo, "Graphene-based materials: Synthesis and gas sorption, storage and separation," *Progress in Materials Science*. 2015, doi: 10.1016/j.pmatsci.2014.10.004.

[41] F. Guo, M. Creighton, Y. Chen, R. Hurt, and I. Külaots, "Porous structures in stacked, crumpled and pillared graphene-based 3D materials," *Carbon N. Y.*, 2014, doi: 10.1016/j.carbon.2013.09.024.

[42] D. R. Dreyer, S. Park, C. W. Bielawski, and R. S. Ruoff, "Graphite oxide," *Chem. Soc. Rev.*, 2010, doi: 10.1039/b917103g.

[43] H.-L. Guo, X.-F. Wang, Q.-Y. Qian, F.-B. Wang, and X.-H. Xia, "A Green Approach to the Synthesis of Graphene Nanosheets," *ACS Nano*, 2009, doi: 10.1021/nn900227d.

[44] A. C. Ferrari and D. M. Basko, "Raman spectroscopy as a versatile tool for studying the properties of graphene," *Nature Nanotechnology*. 2013, doi: 10.1038/nnano.2013.46.

[45] S. Eigler, C. Dotzer, and A. Hirsch, "Visualization of defect densities in reduced graphene oxide," *Carbon N. Y.*, 2012, doi: 10.1016/j.carbon.2012.03.039.

[46] S. Colonna, O. Monticelli, J. Gomez, G. Saracco, and A. Fina, "Morphology and properties evolution upon ring-opening polymerization during extrusion of cyclic butylene terephthalate and graphene-related-materials into thermally conductive nanocomposites," *Eur. Polym. J.*, 2017, doi: 10.1016/j.eurpolymj.2017.02.011.

[47] Y. Katoh and M. Okamoto, "Crystallization controlled by layered silicates in nylon 6-clay nano-composite," *Polymer (Guildf).*, 2009, doi: 10.1016/j.polymer.2009.07.019.

[48]  R. Kumar Mishra, S. Thomas, and N. Karikal, *Micro and Nano Fibrillar Composites (MFCs and NFCs) from Polymer Blends*. 2017.

[49]  J. Tung, R. K. Gupta, G. P. Simon, G. H. Edward, and S. N. Bhattacharya, "Rheological and mechanical comparative study of in situ polymerized and melt-blended nylon 6 nanocomposites," *Polymer (Guildf).*, 2005, doi: 10.1016/j.polymer.2005.08.043.

[50]  A. J. Glover, M. Cai, K. R. Overdeep, D. E. Kranbuehl, and H. C. Schniepp, "In situ reduction of graphene oxide in polymers," *Macromolecules*, 2011, doi: 10.1021/ma2008783.

[51]  S. Ye, D. Hu, Q. Zhang, J. Fan, B. Chen, and J. Feng, "Flow-induced enhancement of in situ thermal reduction of graphene oxide during the melt-processing of polymer nanocomposites," *J. Phys. Chem. C*, 2014, doi: 10.1021/jp5074335.

[52]  E. E. Ferg and L. L. Bolo, "A correlation between the variable melt flow index and the molecular mass distribution of virgin and recycled polypropylene used in the manufacturing of battery cases," *Polym. Test.*, 2013, doi: 10.1016/j.polymertesting.2013.09.009.

[53]  L. Altay *et al.*, "Synergistic effects of graphene nanoplatelets in thermally conductive synthetic graphite filled polypropylene composite," *Polym. Compos.*, 2019, doi: 10.1002/pc.24643.

[54]  J. M. Augustine, S. N. Maiti, and A. K. Gupta, "Mechanical properties and crystallization behavior of toughened polyamide-6/carbon nanotube composites," *J. Appl. Polym. Sci.*, 2012, doi: 10.1002/app.33975.

[55]  T. D. Fornes and D. R. Paul, "Crystallization behavior of nylon 6 nanocomposites,"

*Polymer.*, 2003, doi: 10.1016/S0032-3861(03)00344-6.

[56] H. Wiebeck, D. F. Borrelly, C. Xavier, P. S. Santos, S. A. Asciutti, and M. P. Correa, "The effect of silane coupling agents on a composite polyamide-6/talc," *Brazilian J. Chem. Eng.*, 1998, doi: 10.1590/S0104-66321998000400009.

[57] H. Risite, K. E. L. Mabrouk, M. Bousmina, and O. Fassi-Fehri, "The effect of 3-aminopropyltriethoxysilane on rheological and mechanical properties of polyamide 11/clay nanocomposites," *J. Nanosci. Nanotechnol.*, 2016, doi: 10.1166/jnn.2016.12154.

[58] X. Wang, E. N. Kalali, and D. Y. Wang, "An in situ polymerization approach for functionalized MoS2/nylon-6 nanocomposites with enhanced mechanical properties and thermal stability," *J. Mater. Chem. A*, 2015, doi: 10.1039/c5ta06071k.

[59] J. Chen, B. D. Beake, G. A. Bell, Y. Tait, and F. Gao, "Investigation of the nanomechanical properties of nylon 6 and nylon 6/clay nanocomposites at sub-ambient temperatures," *J. Exp. Nanosci.*, 2016, doi: 10.1080/17458080.2015.1136847.

[60] D. P. N. Vlasveld, S. G. Vaidya, H. E. N. Bersee, and S. J. Picken, "A comparison of the temperature dependence of the modulus, yield stress and ductility of nanocomposites based on high and low MW PA6 and PA66," *Polymer (Guildf).*, 2005, doi: 10.1016/j.polymer.2005.02.094.

[61] S. Pan, M. Sokoluk, C. Cao, Z. Guan, and X. Li, "Facile fabrication and enhanced properties of Cu-40 wt% Zn/WC nanocomposite," *J. Alloys Compd.*, 2019, doi: 10.1016/j.jallcom.2019.01.022.

[62] X. Y. Ji, Y. P. Cao, and X. Q. Feng, "Micromechanics prediction of the effective elastic moduli of graphene sheet-reinforced polymer nanocomposites," *Model. Simul. Mater.*

*Sci. Eng.*, 2010, doi: 10.1088/0965-0393/18/4/045005.

[63]   L. Gong, R. J. Young, I. A. Kinloch, I. Riaz, R. Jalil, and K. S. Novoselov, "Optimizing the reinforcement of polymer-based nanocomposites by graphene," *ACS Nano*, 2012, doi: 10.1021/nn203917d.

[64]   C. Vallés *et al.*, "PMMA-grafted graphene nanoplatelets to reinforce the mechanical and thermal properties of PMMA composites," *Carbon N. Y.*, 2020, doi: 10.1016/j.carbon.2019.10.075.

[65]   D. G. Papageorgiou, I. A. Kinloch, and R. J. Young, "Mechanical properties of graphene and graphene-based nanocomposites," *Progress in Materials Science*. 2017, doi: 10.1016/j.pmatsci.2017.07.004.

**Declaration of interests**

☒ The authors declare that they have no known competing financial interests or personal relationships that could have appeared to influence the work reported in this paper.

☐The authors declare the following financial interests/personal relationships which may be considered as potential competing interests: